Friction mechanisms of graphite from a single-atomic tip to a large-area flake tip

Kouji Miura,[1,*] Naruo Sasaki,[2,3] and Shu Kamiya[1]

[1]*Department of Physics, Aichi University of Education, Hirosawa 1, Igaya-cho, Kariya 448-8542, Japan*

[2]*Department of Applied Physics, Faculty of Engineering, Seikei University, 3-3-1, Kichijoji Kitamachi, Musashino-shi, Tokyo 180-8633, Japan*

[3]*Precursory Research for Embryonic Science and Technology (PRESTO), Japan Science and Technology Agency (JST), 4-1-8 Honcho, Kawaguchi-shi, Saitama 332-0012, Japan*

The frictional mechanisms of graphite derived from a single-atom tip and a graphite flake tip are systematically studied. The frictional forces in both cases are approximately proportional to the loading force because of significant deformation of the graphite surface. For ''atomic friction (single-atom tip),'' the effect of water on the loading force is discussed. The deformation and effective lateral stiffness of the graphite surface under ambient conditions are evaluated using the ''extended Hertz model.'' A single-atom tip attached to the macroscopic tip gives interpretations of atomic resolution of frictional force maps even under high loading conditions. For ''flake friction (flake tip),'' the graphite flake moves on graphite such that the stacking of graphite layers is maintained. In this case, the frictional coefficient along the $[12\bar{3}0]$ direction of the graphite(0001) surface is estimated to be approximately 0.001. The anisotropy of the frictional force as a function of the pulling direction is also shown.

I. INTRODUCTION

Since Mate *et al.*[1] discovered the nanoscale periodic frictional force map of a graphite surface using a tungsten tip in 1987, many studies on atomic-scale friction have been conducted experimentally and theoretically. However, until now, the periodic frictional-force map presented by Mate *et al.* has not been reproduced. In contrast, atomic-scale periodic frictional-force maps different from that presented by Mate *et al.* have been experimentally reported and analyzed by other groups.[2–9] Experimentally, these frictional-force maps[2–9] were almost the same but their interpretations were different. At present, theoretical simulation using a tip, on top of which a single atom is attached, is in good agreement with experimental data, indicating that the top of the probe tip stays for a long time on the hollow site (center of a six-carbon ring in the first surface layer) of a graphite surface. However, the simulated loading force ($\simeq 1$ nN) is about two or three orders of magnitude smaller than the experimental one ($\simeq 100$ nN).[4–6] Thus, the origin of the periodic frictional-force maps obtained on graphite has lacked coherence and has remained unclear for more than a decade.

Therefore, in this paper, the following three points are mainly discussed. First, for atomic friction, the load dependence of frictional-force maps and frictional force is presented. Then the effect of water on the loading force, surface deformation, and effective lateral stiffness is clarified. The importance of surface deformation is discussed in order to explain atomic resolution. Effective lateral stiffness is evaluated. Second, for flake friction, general features of the atomic-scale movement of a graphite flake are discussed experimentally and systematically. Third, the transition from atomic friction (derived from the single-atom tip) to flake friction (derived from the flake tip) is clarified. The anisotropy of the frictional force as a function of the pulling direction is also shown.

II. EXPERIMENT AND SIMULATION

A graphite substrate was prepared by cleaving highly oriented pyrolytic graphite. A cleaved graphite flake with an area of 1 mm square and a thickness of several micrometers was used. Normal and lateral forces were measured simultaneously under a relative humidity of below 50% at room temperature using a commercially available instrument (Seiko Instruments Inc., SPI-3700). The scan speed was 0.13 m/s. Rectangular silicon cantilevers with normal spring constants of 0.05 N/m were used. Zero normal force is defined as the position at which the cantilever is not bent. The frictional forces were calibrated by using the method of Meyer *et al.*[10]

The simulation for atomic friction was performed by scanning the single-atom tip connected with the cantilever spring on a graphite monolayer surface. The model of the graphite monolayer surface consists of 600 carbon atoms and 271 hexagons. The lattice constant of graphite is assumed to be 1.421 Å. The details of the model have already been described in the previous works by Sasaki *et al.*[4–6]

III. ATOMIC FRICTION

A. Frictional-force maps

Figure 1 shows the experimental and simulated frictional-force maps for two different loading forces. F^x and F^y are x and y components of lateral forces, obtained by scanning the tip along the x direction, as shown in Fig. 1. As illustrated in the right part of Fig. 1, the load F_L^z, comprised of the short-range component F_{sr}^z and the long-range one F_{lr}^z, can be given as

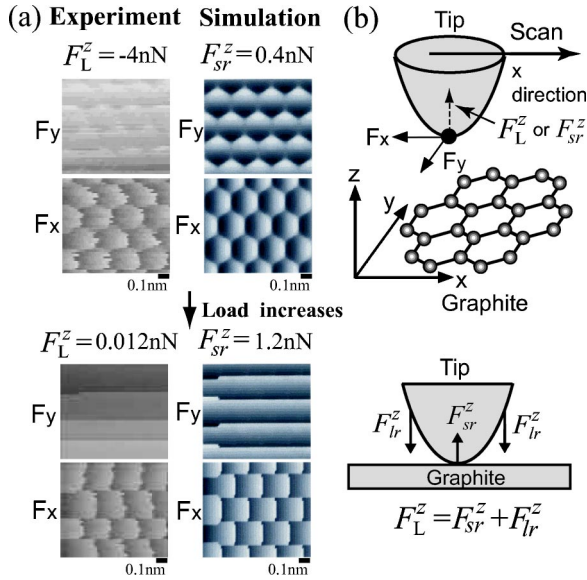$$F_L^z = F_{sr}^z + F_{lr}^z. \tag{1}$$

FIG. 1. (a) The experimental and simulated frictional maps of graphite acting on a tip along the x and y directions under the constant-force mode at two different loading forces. $F_L^z = -4$ nN(experiment) corresponds to $F_{sr}^z = 0.4$ nN(simulation), and $F_L^z = 0.012$ nN(experiment) corresponds to $F_{sr}^z = 1.2$ nN(simulation). (b) Schematic illustration of the tip and surface system with a definition of F_x, F_y, and F_L^z comprised of F_{lr}^z and F_{sr}^z.

F_L^z is obtained by calculating the equilibrium position of the tip considering the surface stiffness. Therefore F_L^z implicitly includes information on surface stiffness. First, F_{sr}^z is obtained by theoretical simulation, where the long-range force is not considered.[3-6] Next, F_{lr}^z, the long-range component of F_L^z, is comprised of van der Waals and capillary forces. First, it can be clearly seen that the experimental image patterns are in very good agreement with the simulated ones, and change significantly depending on the load. At a lower loading force ($F_L^z = -4$ nN), the zigzag pattern corresponding to the C-C bond of the graphite lattice appears. However, as the load increases ($F_L^z = 0.012$ nN), this zigzag pattern vanishes and only the straight pattern parallel to the scan direction appears. Subsequently, frictional-force patterns remain almost constant when the loading force F_L^z becomes larger than 0.012 nN. The reason for this will be discussed later.

Figure 2 shows the tip position (X) as a function of the lever support position (X_s) for scan lines A and B. Scan lines A and B correspond to lines along the hollow sites and the carbon atoms, respectively. The results of experiment are clearly in very good agreement with those of the simulation. At a lower loading force ($F_L^z = -4$ nN in the experiment corresponding to $F_{sr}^z = 0.4$ nN in the simulation), for scan line A, the tip movement is discrete with the periodicity of 2.46 Å. However, for scan line B, the tip movement is smoothly continuous. This is due to the fact that the effective spring constant within the x-y plane for scan line B becomes larger than that for scan line A, because, when the tip is scanned on scan line B, the cantilever spring constant has an additional y component. Thus energy dissipations due to

stick-slip motion do not always exist for the lower loading force ($F_L^z = -4$ nN), as shown in scan line B in Fig. 2.

This feature corresponds to the results of no energy dissipation obtained theoretically by Tomank et al.[11] However, this does not necessarily mean that the frictional force during the scan is zero, even though the mean frictional force becomes zero. Here, let us consider the possibility of zero frictional force. When a paired tip is assumed to be scanned, one tip climbs and the other tip descends the mountain of an interaction potential, which produces an extremely small load without energy dissipation. It can be expected that such a system will exhibit zero kinetic frictional force during quasistatic sliding. It is interesting to note that further development of this discussion leads to friction between surfaces, as discussed for the Frenkel-Kontorova-Tomlinson system.[12]

B. Effect of water on the loading force

Here, it should be noted that, experimental loading forces in our experiment are much smaller than those reported by Fujisawa et al.[7,8] The reason for this is ascribed to the amount of water covering the graphite surface, which makes F_{lr}^z larger than that of Fujisawa et al.[7,8] F_{lr}^z, the long-range component of F_L^z, strongly depends on the environment, particularly the amount of water on the sample surface. Therefore the effect of water on F_{lr}^z is discussed below. Under an ultrahigh-vacuum condition, when there is no water on the surface, F_{lr}^z is mainly described by the van der Waals interaction force obtained by Goodman and Garcia[13] for the atomic force microscope (AFM) tip with radius of curvature R, in the case of $z \ll R$, as

$$F_{lr}^z(\text{UHV}) = -\frac{3}{4}K\beta_S\beta_T\frac{R}{z^2}, \qquad (2)$$

where $K = 1.41$ eV is a universal constant determined by Hoinkes[14] from experimental He surface scattering data, and $\beta_S \simeq 0.592$ and $\beta_T \simeq 0.118$ are constants related to the dielectric constants of the graphite sample and the SiO$_2$ tip, respectively, calculated using the Clausius-Mossotti formula.

Under ambient conditions, when the sample surface is covered with water, F_{lr}^z is mainly described by the capillary force. In this case, the water meniscus is formed between the tip and graphite surface, which produces an attractive capillary force,

$$F_{lr}^z(\text{air}) = -\frac{4\pi\gamma R\cos\theta}{1 + z/R(1 - \cos\phi)}, \qquad (3)$$

where θ and ϕ are the contact and meniscus angles, respectively,[15] and $\gamma = 0.07$ N/m is the surface tension of water.

Under liquid conditions, when the amount of water on the surface increases considerably (operation of AFM in water), the capillary force mentioned above is greatly reduced. Garcia and Binh[16] have shown that, in the case of $z \ll R$,

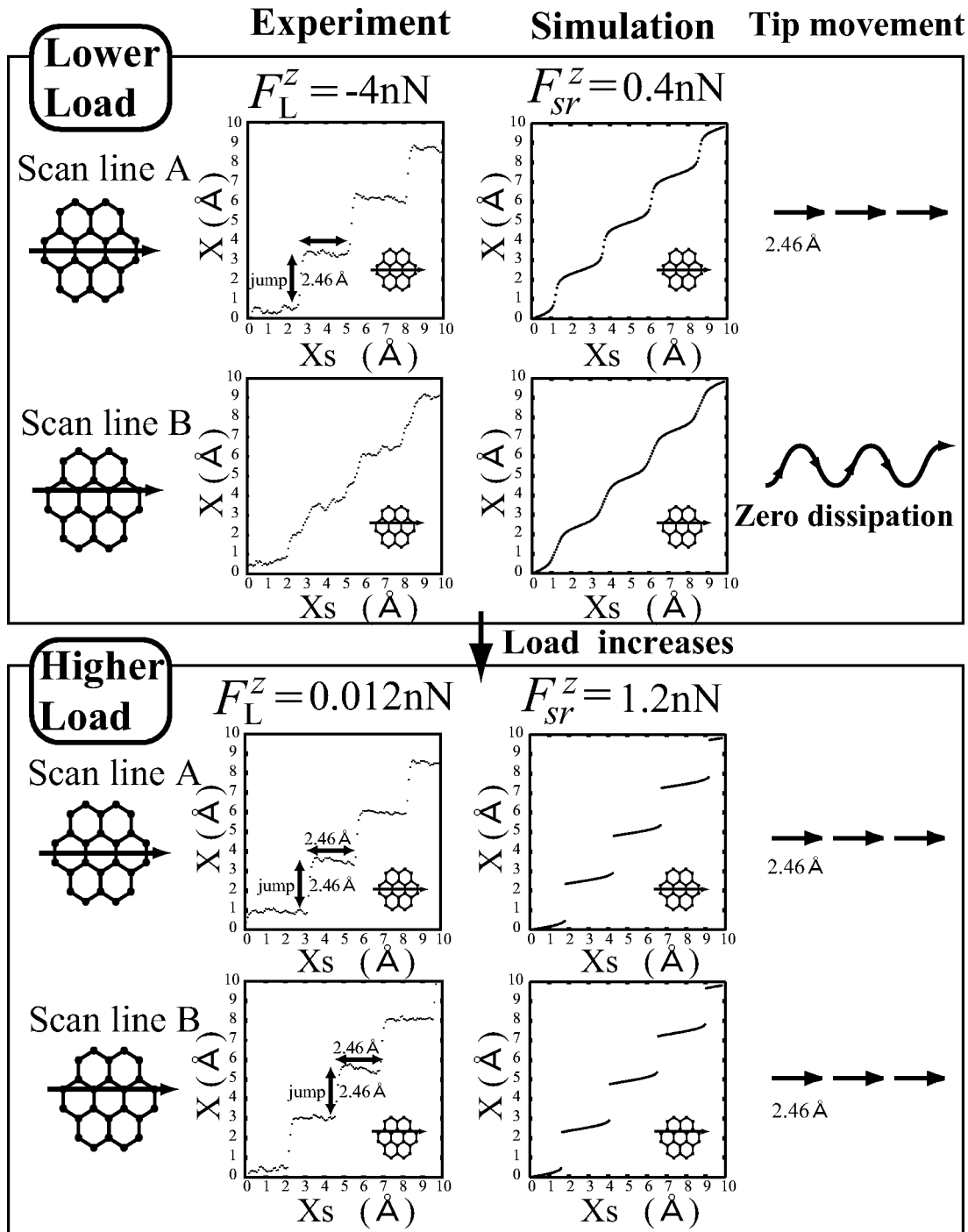$$F_{lr}^z(\text{water}) = -\frac{3}{4}K(\beta_S - \beta_l)\beta_T\frac{R}{z^2}, \qquad (4)$$

FIG. 2. The tip position (X) as a function of the lever support position (X_s) for scan lines A and B. The tip movement is also shown. For each line, experimental and simulated results are shown. As the load increases, a considerable change appears in the case of scan line B.

where $\beta_l \simeq 0.975$ is a constant related to the dielectric constant of water.

Figure 3 shows the effect of water on F_{lr}^z for the case of $R = 20$ nm, the estimated value for the AFM tip used in our experiment. The parameters $\theta = 0°$ and $\phi = 10°$ are substituted into Eq. (3) to calculate capillary force $F_{lr}^z(\text{air})$. As shown in Fig. 3, $F_{lr}^z(\text{air})$ clearly exhibits the largest attractive force. In water, $F_{lr}^z(\text{water})$ becomes repulsive. Since our experiment is performed under ambient conditions, where the

relative humidity is around 50%, it is sufficient to consider $F_{lr}^z(\text{air})$ as a long-range interaction force. It should be noted that calculated $F_{lr}^z(\text{air})$ for $z = 0.2$ nm is about -11 nN, which corresponds well to pull-off forces $F_{\text{pull-off}}^z \simeq -8$ nN measured in our present experiment.

C. Deformation of graphite

Deformation of graphite under ambient conditions is considered. In order to discuss the tip-surface contact during the
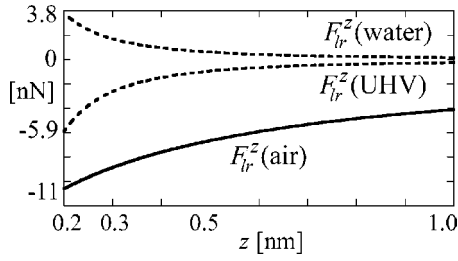
FIG. 3. The long-range force as a function of the tip height z, under UHV condition $F_{lr}^z(\text{UHV})$, ambient condition $F_{lr}^z(\text{air})$, and liquid condition $F_{lr}^z(\text{water})$.

scanning process, the microscopic tip attached to the macroscopic tip is considered, as shown in Fig. 4. R_{macro} and R_{micro} are denoted as the radii of curvature of the macroscopic and microscopic tips, respectively, hereafter. For the macroscopic tip, the contact radius a_{macro} between the tip and the surface and the deformation of graphite d_{macro} under ambient conditions are described using the "extended Hertz model" proposed by Fogden and White,[17]

$$d_{\text{macro}}=\frac{1-\nu_S^2}{E_S}\left[\left(\frac{3F_L^{z,eff}}{4}\right)^2\frac{E^*}{R_{\text{macro}}}\right]^{1/3},$$

$$a_{\text{macro}}=\left(\frac{3R_{\text{macro}}F_L^{z,eff}}{4E^*}\right)^{1/3}, \quad (5)$$

where

$$F_L^{z,eff}=F_L^z-F_{\text{pull-off}}^z, \quad (6)$$

and

$$E^*=\left(\frac{1-\nu_T^2}{E_T}+\frac{1-\nu_S^2}{E_S}\right)^{-1}, \quad (7)$$

are used.[18] Here $R_{\text{macro}}=20$ nm. $F_L^{z,eff}$ is an effective loading force, including the pull-off force $F_{\text{pull-off}}^z\simeq-8$ nN, which is measured in our experiment. Furthermore, $E_T=1.5\times10^{11}$ N/m^2 and $E_S=2.0\times10^{11}$ N/m^2 are Young moduli of the Si$_3$N$_4$ tip and the graphite surface, respectively.[19] $\nu_T=\nu_S\simeq0.3$ are typical values of the Poisson ratio.[19]

Similarly, for the microscopic tip, the relations

$$d_{\text{micro}}=\frac{1-\nu_S^2}{E_S}\left[\left(\frac{3F_{sr}^z}{4}\right)^2\frac{E^*}{R_{\text{micro}}}\right]^{1/3},$$
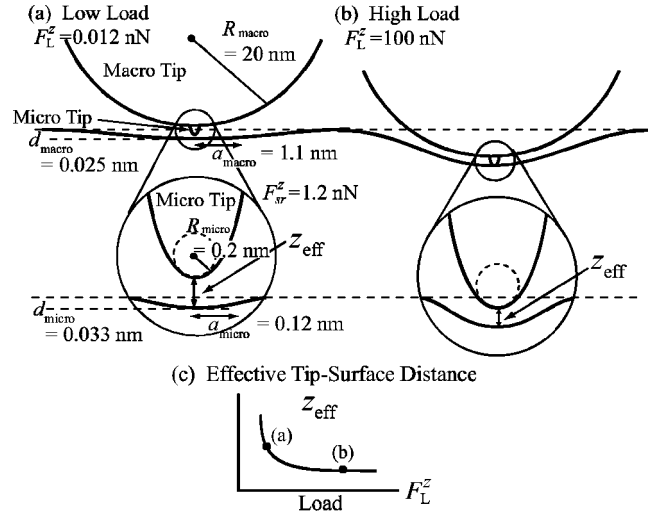

FIG. 4. The microscopic tip attached to the macroscopic tip. (a) For low loading force F_L^z, microscopic deformation d_{micro} is comparable to the macroscopic deformation d_{macro}. (b) For high loading force F_L^z, although macroscopic deformation d_{macro} becomes dominant in the macroscopic scale, the effect of microscopic deformation d_{micro} contributes to the atomic resolution of frictional force image. (c) The effective tip-surface distance z_{eff} as a function of load F_L^z.

$$a_{\text{micro}}=\left(\frac{3R_{\text{micro}}F_{sr}^z}{4E^*}\right)^{1/3}, \quad (8)$$

are used. The microscopic tip represents a single-atom tip with $R_{\text{micro}}=0.2$ nm, which is comparable to the bond length of carbon or silicon.

Table I shows the deformations and contact radii of the graphite for both macroscopic and microscopic tips. As shown in Table I, for the low loading condition of $F_L^z\simeq-4$ and 0.012 nN, corresponding to $F_{sr}^z\simeq0.4$ and 1.2 nN, respectively, both the macroscopic and microscopic tips contribute to the deformation of the tip-surface contact. The microscopic deformation d_{micro} is approximately as large as the macroscopic one, d_{macro}. However, macroscopic contact radii a_{macro} are ten times as large as microscopic ones a_{micro} [Fig. 4(a)]. Considering that the microscopic contacts with a radius of $a_{\text{micro}}=0.086$ and 0.12 nm correspond well to the atomic bond length, this microscopic contact provides atomic-scale information. On the other hand, macroscopic contact with a radius of $a_{\text{macro}}\simeq1$ nm does not yield atomic-scale information but summation of it. It should be noted that the above microscopic deformation d_{micro} has the same order

TABLE I. The deformations and contact radii of graphite for both macro- and microscopic tips. d_{macro} and d_{micro} are graphite deformations for macroscopic and microscopic tips, respectively. a_{macro} and a_{micro} are contact radii for macro- and microscopic tips, respectively.

Macrotip ($R_{\text{macro}}=20$ nm)	d_{macro}	a_{macro}	Microtip ($R_{\text{micro}}=0.2$nm)	d_{micro}	a_{micro}
$F_L^z=-4$ nN	0.016 nm	0.86 nm	$F_{sr}^z=0.4$ nN	0.016 nm	0.086 nm
$F_L^z=0.012$ nN	0.025 nm	1.1 nm	$F_{sr}^z=1.2$ nN	0.033 nm	0.12 nm

of magnitude of that evaluated by Soler *et al.*,[20] which is less than 0.1 nm for the tip height of $z \simeq 0.25$ nm.

For the high loading condition of $F_L^z \simeq 100$ nN, the macroscopic tip plays a major role in the deformation of the tip-surface contact. The deformation by the microscopic tip, d_{micro}, does not increase any longer. The reason for that can be explained as follows: As the tip approaches the surface further, the graphite surface continues to deform so that the effective distance between the microscopic tip and surface, z_{eff}, is kept nearly constant, as shown in Figs. 4(b) and 4(c). This behavior of z_{eff} as a function of the initial tip height z, has already been discussed for the atomic force microscopy system comprised of a diamond tip and graphite surface.[3] z_{eff} decreases negligibly below 2 Å even if the actual tip height z decreases below 2 Å, because the effective spring constant corresponding to the interaction force between the microscopic tip and the surface becomes sufficiently large.

Thus, for both the low and high loading conditions, the microscopic tip contributes to the true atomic resolution of frictional-force maps, because the microscopic tip cannot approach the surface below the certain tip height $z_{eff} \simeq 2$ Å, as mentioned above. This gives us one explanation why periodic frictional features appear even for a higher loading force. (It should be noted that frictional-force maps having the same pattern as in Fig. 1 for the low loading force of $F_L^z = 0.012$ nN are obtained for the high loading force of $F_L^z \simeq 100$ nN.) Another explanation for the periodic features of frictional force maps will be given later in Sec. V A. The friction derived from the single-atom tip is called "atomic friction," hereafter.

Lastly, the following point should be noted: The fact that frictional-force patterns do not change for $F_L^z > 0.012$ nN, as mentioned in Sec. III A, can be explained by the unchangeable situation of the microscopic contact for the high loading conditions, that is to say, $z_{eff} \simeq 2$ Å.

D. Effective lateral stiffness

Figures 5(a) and 5(b) present frictional force F_x and effective lateral stiffness k_{eff}^x as functions of load F_L^z, respectively. As loading force F_L^z increases, the maximum frictional force (solid line) increases and approaches the asymptotic value of $\simeq 4.2$ nN, as shown in Fig. 5(a). However, the mean frictional force (black circles) is quite small, nearly constant. Similarly, as loading force F_L^z increases, the slope of the sticking part k_{eff}^x increases monotonically and approaches the asymptotic value, $k_{eff}^x \simeq 38$ N/m, for $F_L^z \gtrsim 150$ nN, as shown in Fig. 5(b). This behavior of k_{eff}^x can be explained as follows.

First, the effective lateral stiffness k_{eff}^x of the cantilever-tip-surface system can be described as

$$k_{eff}^x = (1/k_{contact}^x + 1/k_{tip}^x + 1/k_{lever}^x)^{-1}, \qquad (9)$$

where $k_{contact}^x$, k_{tip}^x, and k_{lever}^x, are, lateral sample stiffness, lateral tip stiffness, and lateral cantilever stiffness, respectively,[21–23] as shown in Fig. 5(c).
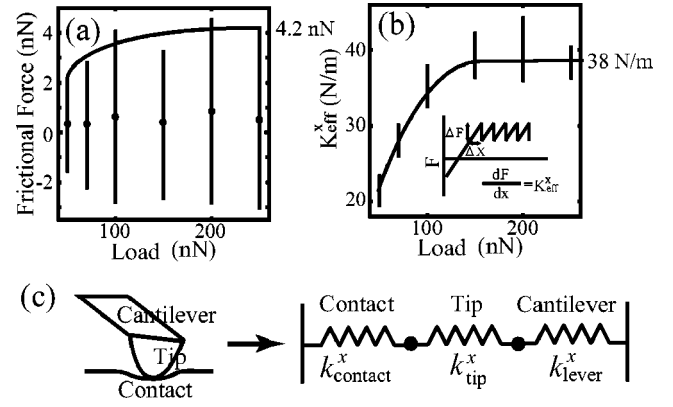

FIG. 5. (a) Frictional force as a function of loading force. The bars and black circles indicate the stick-slip amplitudes and the mean frictional forces, respectively. (b) Effective lateral stiffness k_{eff}^x as a function of loading force. (c) The tip-surface system can be described by the spring model with the spring constants of k_{lever}^x, k_{tip}^x, and $k_{contact}^x$.

Second, $k_{contact}^x$ under ambient conditions is obtained using the extended Hertz model[17] mentioned in the preceding section, such as

$$k_{contact}^x \propto (F_L^{z,eff})^{1/3} = (F_L^z - F_{pull-off}^z)^{1/3}, \qquad (10)$$

where $F_L^{z,eff}$ is effective loading force considering the pull-off force $F_{pull-off}^z \simeq -8$ nN measured in our experiment.

Thus, substitution of Eq. (10) into Eq. (9), explains the behavior of k_{eff}^x in Fig. 5(b) in the following two points. (1) k_{eff}^x monotonically increases as the load F_L^z increases. (2) When F_L^z finally becomes large enough, the effect of $1/k_{contact}^x$ can be neglected, and k_{eff}^x can be expected to approach an asymptotic value

$$k_{eff}^x \rightarrow (1/k_{tip}^x + 1/k_{lever}^x)^{-1} \rightarrow 37 \ \text{N/m}, \qquad (11)$$

where the values of $k_{lever}^x = 650$ N/m (torsional stiffness of cantilever used in our experiment) and $k_{tip}^x = 39$ N/m (value of Si_3N_4 calculated by Lantz *et al.*[22]) are used. This evaluated value of $k_{eff}^x = 37$ N/m is in good agreement with our experimental value of $k_{eff}^x = 38$ N/m. Thus the torsional deformation of the tip and cantilever significantly influence the lateral stiffness for a large load F_L^z. In particular, the effect of the tip stiffness is dominant.

IV. FLAKE FRICTION

Figure 6 shows two frictional-force maps obtained by scanning the graphite flake along the x direction on different areas of the graphite surface. First, frictional image patterns gradually change during scanning the tip from top to bottom. The size of the unit cell at the bottom is larger than that at the top. Next, three different types of image patterns, *A*, *B*, and *C*, are obtained. Furthermore, it is shown that scalelike frictional maps in Fig. 6, are clearly different from those for "single-atom friction." For the case where the flake is scanned by the tip, there are two different kinds of frictional mechanisms. One is the friction acting between a tip and a
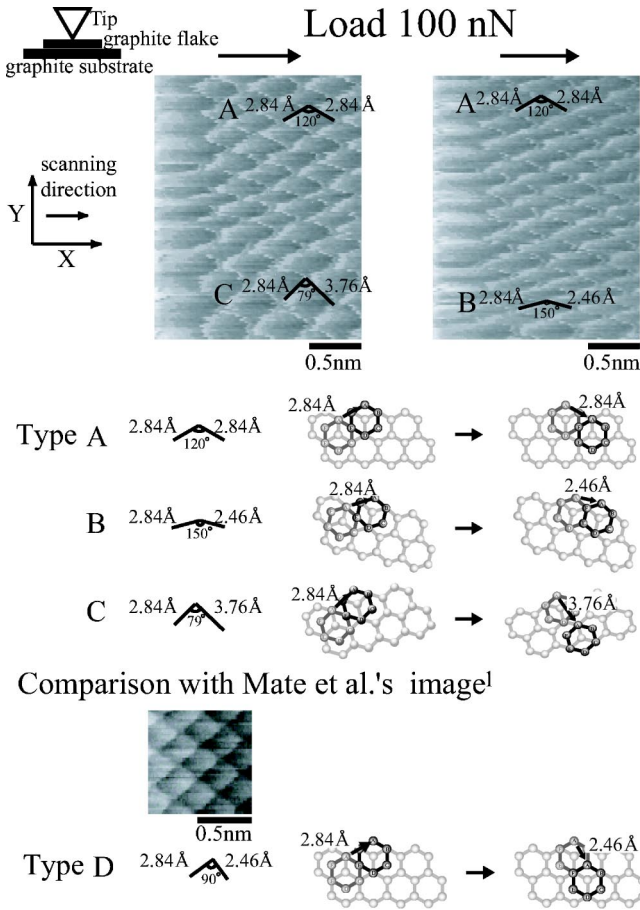
FIG. 6. Two kinds of frictional-force maps of graphite obtained by scanning the graphite flake along the x direction, where the arrows indicate the scanning direction. The three types $(A-C)$ of movement of the graphite flake are shown in the lower part of figure. As a comparison, type D obtained by Mate *et al.* (Ref. 1) is also shown.

FIG. 7. (a) Effective potential of a graphite flake on the graphite surface. (b) Experimental and simulated images for type A in Fig. 6.

graphite flake, and the other is that acting between a graphite flake and the graphite surface. Here the feature in the frictional-force map for the single-atom tip (Fig. 1) does not appear in Fig. 6. Therefore it is reasonable to conclude that Fig. 6 shows only the frictional feature of the flake scanned on the graphite surface. This also indicates that the friction between a tip and a graphite flake is larger than that between a graphite flake and a graphite surface. Thus, when the tip is scanned, the graphite flake moves together with the tip. Hereafter a tip with a graphite flake is called a "flake tip."

The frictional-force maps obtained using a flake tip are classified into three types $(A-C)$, according to the movement of the graphite flake $(A-C)$ as shown in the lower part of Fig. 6. Here, we explain the type A frictional-force map, which is the standard pattern in this experiment. The movement of the flake on the graphite surface is converted to the movement of a center of the flake mass with a constant velocity in the effective potential as follows: $V = V_0\{2 \cos[(2\pi/a)x]\cos[(2\pi/a\sqrt{3})y] + \cos[(4\pi/a\sqrt{3})y]\}$, where $a = 0.142$ nm $\times 2 = 0.284$ nm. This effective potential is determined such that it takes the minimum value at the natural stacking position of graphite, as shown in Fig. 7(a).
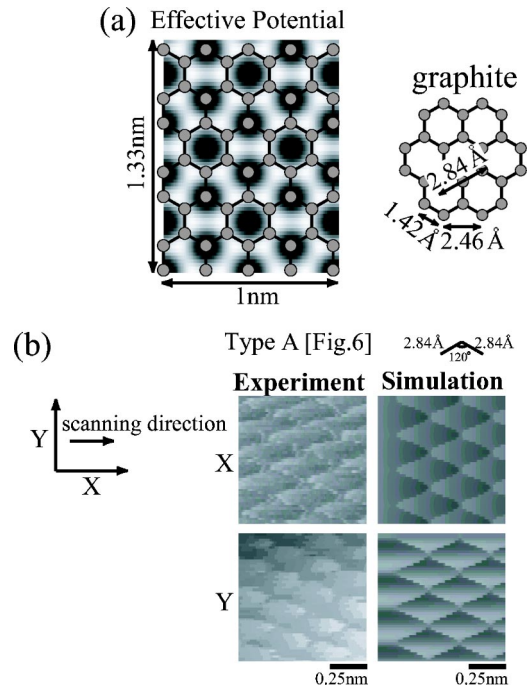
The result of this simple preliminary simulation reproduces the experimental frictional-force image of type A quite well, as shown in Fig. 7(b). Here, the spacing of $a = 0.284$ nm indicates the distance from the present to the next stable position where AB stacking of graphite is maintained. Similarly, the other patterns, B and C, reveal that flake movement is also carried out so as to maintain the AB stacking of graphite, as shown in Fig. 6. As a comparison, the frictional-force map by Mate *et al.*[1] is shown as type D in Fig. 6, which can be explained by another movement of the graphite flake.

Here, the number of carbon atoms contributing to interlayer sliding N_c is evaluated. Since the frictional force F_{flake} is of the order of nanonewtons, the energetic barrier for the interlayer sliding in this experiment, Δ_{total}, is evaluated as follows: $\Delta_{total} = F_{flake} \times a(\text{spacing}) \simeq \text{nN} \times 0.1$ nm $\simeq$ eV. Furthermore, it has been reported that the energetic barrier (the energy difference between AA stacking and AB stacking of graphite) for interlayer sliding, Δ_{atom}, is approximately 12 meV per carbon atom.[24] Therefore, the number of carbon atoms contributing to interlayer sliding is $N_c = \Delta_{total}/\Delta_{atom} \simeq \text{eV}/12$ meV $\simeq 100$, which corresponds to a circle with a radius $\simeq 0.856$ nm of a cluster including 96 carbon atoms, as shown in Fig. 8. Thus the actual contact area between the graphite flake and graphite surface becomes very small, compared to the total area of the flake, 1 mm square.

Figure 9 shows the flake position as a function of the lever support position. Unlike the case in Fig. 2 for atomic friction, Fig. 9 for flake friction exhibits sharp peaks for the slip process. As discussed in Sec. III A, this feature is also identical to that given theoretically by Tomanék *et al.*,[11] which indicates no jump (or no energy dissipation) when the flake moves on the graphite substrate. This suggests that driving force (a static frictional force) arises when the flake
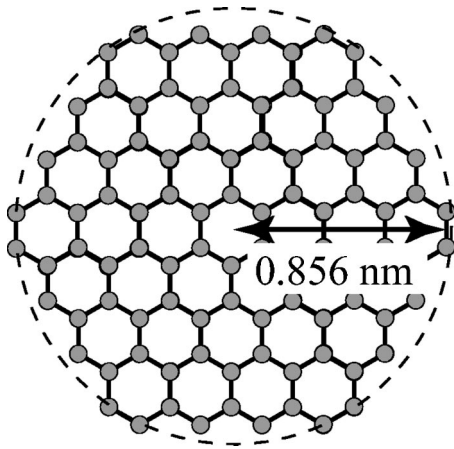
FIG. 8. The contact area with a radius $\simeq 0.856$ nm of a carbon cluster including 96 atoms, which is negligible compared to the total area of the flake, 1 mm square.

moves on the graphite surface but dynamical frictional force disappears. We believe that this gives an explanation of why the friction of a system that includes various flakes is generally small, e.g., friction force acting on many flakes with different movements may be close to zero.

More detailed numerical simulation of flake dynamics are being performed by Matsushita, Matsukawa, and Sasaki.[25] It is shown that the stick-slip motion of a flake is due to the binding of a flake close to the AB stacking configurations of the graphite substrate, which will be reported elsewhere.

V. SIMILARITIES AND DIFFERENCES BETWEEN ATOMIC FRICTION AND FLAKE FRICTION

A. Similarities and differences

Figure 10 presents frictional force as a function of loading force for atomic [Figs. 10(a) and 10(b)] and flake friction [Figs. 10(c) and 10(d)]. For atomic friction, friction coefficients μ_{Ap} and μ_{Az} corresponding to "atom-parallel" [Fig. 10(a)] and "atom-zigzag" [Fig. 10(b)], respectively, are estimated to be approximately 0.001.

Next, for "flake-parallel" [Fig. 10(c)], the graphite (0001) flake moves parallel to the scan direction, which is along the $[12\bar{3}0]$ crystallographic axis. The frictional force is very weakly proportional to the loading force. The proportional
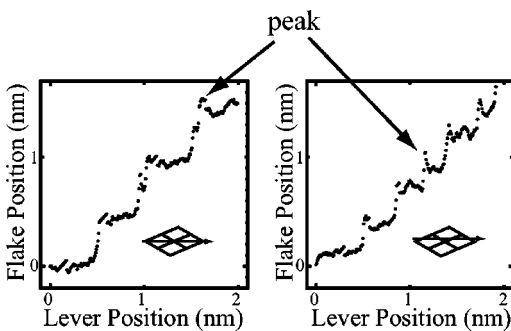

FIG. 9. The flake position as a function of the lever support position for different scan lines in the scalelike patterns.
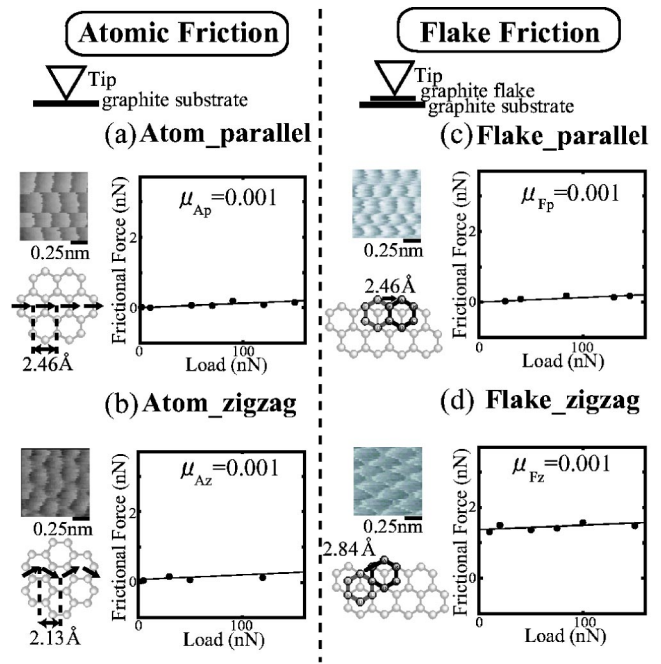

FIG. 10. The mean frictional forces as a function of loading force for atomic friction [(a) atom-parallel and (b) atom-zigzag on the left-hand side] and for flake friction [(c) flake-parallel and (d) flake-zigzag on the right-hand side]. The frictional-force maps and the tip movement corresponding to each case are also presented.

coefficient μ_{Fp} is estimated to be approximately 0.001, which corresponds to the friction coefficient $\mu_{12\bar{3}0}$. However, for "flake-zigzag" [Fig. 10(d)], corresponding to type A in Fig. 6, the graphite flake motion is zigzag, not parallel to the scan direction. The frictional force F_x satisfies the relationship $F_x = \alpha + \mu_{Fz}F_L^z$, where $\alpha = 1.3$ nN and $\mu_{Fz} = 0.001$.

Here it should be noted that the case of flake-parallel [Fig. 10(c)] is energetically more favorable than the case of flake-zigzag [Fig. 10(d)], because, for flake-parallel, AA stacking never appears within the shortest path along the $[12\bar{3}0]$ direction. This simply means the graphite flake easily shears along the $[12\bar{3}0]$ direction on the graphite (0001) surface. On the other hand, for flake-zigzag, AA stacking always appears within the shortest path of flake movement. Thus the energetic barrier during the shear along the $[12\bar{3}0]$ direction is smaller than in the case of flake-zigzag.

The transition from atom-parallel [Fig. 10(a)] to flake-parallel [Fig. 10(c)] corresponds to the change in the frictional mechanism from atomic friction to flake friction. The transition from atom-zigzag [Fig. 10(b)] to flake-zigzag [Fig. 10(d)] also corresponds to the same change as above.

Comparisons between Figs. 10(a) and 10(c), and Figs. 10(b) and 10(d), provide important information for the interpretation of frictional-force maps. For the parallel motion, it should be noted that the frictional-force pattern in Fig. 10(a) is identical to that in Fig. 10(c). Thus, we found that the same frictional-force patterns are obtained with the single-atom tip and the flake tip. This indicates that it is difficult to check whether the periodic frictional-force pattern exhibits
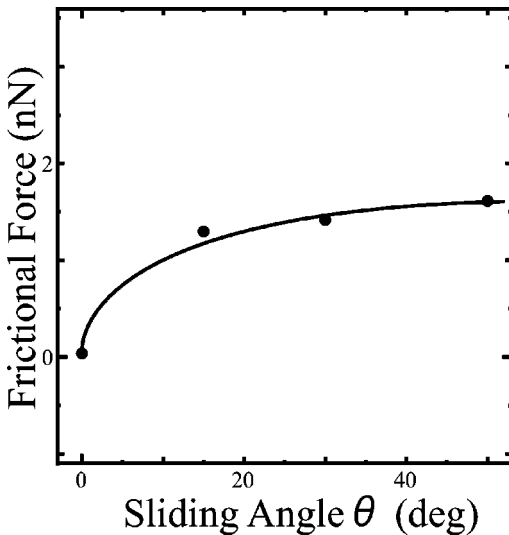
FIG. 11. The mean frictional force as a function of sliding angle θ for a loading force of 100 nN.

true atomic resolution or not. On the other hand, for the zigzag motion, Fig. 10(b) is clearly different from Fig. 10(d).

B. Anisotropy of frictional force

Figure 11 shows the anisotropy of the frictional force as a function of the pulling direction. The sliding angle θ is denoted as the angle between the direction of flake movement and the pulling direction. The frictional forces increase as the sliding angle increases, which, interestingly, is similar to the behavior of the frictional force between flat surfaces discussed by Gyalog and Thomas.[26]

These results lead to the following two points: (i) in the case where the flake moves parallel to the pulling direction, the frictional force is the smallest; (ii) in the case where the flake does not move parallel to the pulling direction, the flake does not move toward the next stable point until the projection of the pulling force coincides with the force which causes the flake to begin moving. Thus, as the sliding angle becomes larger, the pulling force becomes larger. Here, it should be noted that preferred sliding directions have been observed in MoO_3 nanocrystals on MoS_2 surfaces[27] and MoS_2 flakes on MoS_2 surfaces.[28] Recently we found that the graphite/C_{60}/graphite system exhibits zero dynamic friction, which has opened a new research area of molecular bearings.[29] Thus, it is very interesting to note that these findings provide us important information on how to decrease friction between surfaces.

VI. CONCLUSION

This study clarifies the change in the frictional mechanism from atomic friction to flake friction. For atomic friction, frictional-force maps changed significantly at extremely small loads, whereas they remained constant at large load. Atomic friction under ambient conditions was discussed. In this case, the effect of water was significant, and capillary force gave the same order of magnitude of pull-off force as observed experimentally. The deformation of the graphite surface and effective lateral stiffness under ambient conditions were evaluated using the extended Hertz model. The calculated microscopic deformation was in good agreement with that reported by Soler et al.[20] The calculated effective lateral stiffness could explain our experimental results. Furthermore, the small friction coefficient of 0.001 and atomic resolution were ascribed to the surface deformations, where the space between the tip and surface was kept constant. Thus a single-atom tip attached to a macroscopic tip enabled reasonable representations of the atomic resolution of frictional force maps even under high loading conditions.

Next flake friction was discussed. In this case, the graphite flake moved on the graphite surface such that the stacking of graphite layers was maintained. For the case where the flake movement was parallel to the pulling direction, the frictional-force was the smallest. Thus, the friction coefficient for flake friction along the pulling direction $[12\bar{3}0]$ of the graphite(0001) surface was estimated to be approximately 0.001. For the case where the direction of flake movement was not parallel to the pulling direction, the flake did not begin to move toward the next stable point until the projection of the pulling force became coincident with the force which caused the flake to begin moving.

The insensitivity of the frictional force to loading force revealed that surface deformations play an important role in flake friction, similarly to the case of atomic friction. Furthermore, the zigzag movement of the flake should induce a rotation of the flake around a pivot point, in addition to simple translation. In order to confirm the rotation of a flake and self-lubrication by lowering of the energy barrier, detailed analysis of elastic materials including atomic displacement are needed. Numerical simulation of flake dynamics are being performed by Matsushita, Matsukawa, and Sasaki,[25,30] which shows that the stick-slip motion of a flake is due to the binding of a flake close to the AB stacking configurations of the graphite substrate and the mechanism of low friction, considering the effect of temperature.[25,30]

ACKNOWLEDGMENT

*Corresponding author. Email address: kmiura@auecc.aichi-edu.ac.jp

[1] C.M. Mate, G.M. McClelland, R. Erlandsson, and S. Chiang, Phys. Rev. Lett. **59**, 1942 (1987).

[2] J. Ruan and B. Bhushan, J. Appl. Phys. **76**, 5022 (1994).

[3] N. Sasaki and M. Tsukada, Phys. Rev. B **52**, 8471 (1995).

[4] N. Sasaki, K. Kobayashi, and M. Tsukada, Phys. Rev. B **54**, 2138 (1996).

[5] N. Sasaki, M. Tsukada, S. Fujisawa, Y. Sugawara, S. Morita, and K. Kobayashi, J. Vac. Sci. Technol. B **15**, 1479 (1997).

[6] N. Sasaki, M. Tsukada, S. Fujisawa, Y. Sugawara, S. Morita, and K. Kobayashi, Phys. Rev. B **57**, 3785 (1998).

[7] S. Morita, S. Fujisawa, and Y. Sugawara, Surf. Sci. Rep. **23**, 1 (1996).

[8] S. Fujisawa, K. Yokoyama, Y. Sugawara, and S. Morita, Phys. Rev. B **58**, 4909 (1998).

[9] H. Hölscher, U.D. Schwarz, O. Zworner, and R. Wiesendanger, Phys. Rev. B **57**, 2477 (1998).

[10] E. Meyer, R. M. Overney, K. Dransfeld, T. Gyalog, *Nanoscience: Friction and Rheology on the Nanometer Scale* (World Scientific, Singapore, 1999), p. 349.

[11] D. Tomanék, W. Zhong, and H. Thomas, Europhys. Lett. **15**, 887 (1991).

[12] M. Weiss and F.-J. Elmer, Phys. Rev. B **53**, 7539 (1996).

[13] F.O. Goodman and N. Garcia, Phys. Rev. B **43**, 4728 (1991).

[14] H. Hoinkes, Rev. Mod. Phys. **52**, 933 (1980).

[15] J. N. Israelachvili, *Intermolecular and Surface Forces* (Academic Press, London, 1985).

[16] N. Garcia and V.T. Binh, Phys. Rev. B **46**, 7946 (1992).

[17] A. Fogden and L.R. White, J. Colloid Interface Sci. **138**, 414 (1990).

[18] L. D. Landau and E. M. Lifshitz, *Course of Theoretical Physics: Theory of Elasticity*, 3rd ed. (Butterworth-Heinemann, London, 1995), Vol. 7.

[19] D. Sarid, *Scanning Force Microscopy: Revised Edition* (Oxford, New York, 1994).

[20] J.M. Soler, A.M. Baro, N. Garcia, and H. Rohrer, Phys. Rev. Lett. **57**, 444 (1986).

[21] R.W. Carpick, D.F. Ogletree, and M. Salmeron, Appl. Phys. Lett. **70**, 1548 (1997).

[22] M.A. Lantz, S.J. O'Shea, A.C.F. Hoole, and M.E. Welland, Appl. Phys. Lett. **70**, 970 (1997).

[23] S. Okita and K. Miura, Surf. Sci. **442**, L959 (1999).

[24] J.-C. Chalier, X. Gonze, and J.-P. Michenaud, Europhys. Lett. **28**, 403 (1994).

[25] K. Matsushita, H. Matsukawa, and N. Sasaki, cond-mat/0307474v1 (unpublished).

[26] T. Gyalog and H. Thomas, Europhys. Lett. **37**, 195 (1997).

[27] P.E. Sheehan and C.M. Lieber, Science **272**, 1158 (1996).

[28] K. Miura and S. Kamiya, Europhys. Lett. **58**, 610 (2002).

[29] K. Miura, S. Kamiya, and N. Sasaki, Phys. Rev. Lett. **90**, 055509 (2003).

[30] K. Matsushita (private communication).